

---

This is an electronic reprint of the original article.  
This reprint may differ from the original in pagination and typographic detail.

Bannmann, S.; Bozhenkov, S.; Äkäslompolo, S.; Poloskei, P.; Schneider, W.; Ford, O.; Wolf, R. C.; W7-X Team

## Feasibility of neutral particle analysis for fast-ion measurements at W7-X

*Published in:*  
Journal of Instrumentation

*DOI:*  
[10.1088/1748-0221/17/01/P01034](https://doi.org/10.1088/1748-0221/17/01/P01034)

Published: 01/01/2022

*Document Version*  
Publisher's PDF, also known as Version of record

*Published under the following license:*  
CC BY

*Please cite the original version:*  
Bannmann, S., Bozhenkov, S., Äkäslompolo, S., Poloskei, P., Schneider, W., Ford, O., Wolf, R. C., & W7-X Team (2022). Feasibility of neutral particle analysis for fast-ion measurements at W7-X. *Journal of Instrumentation*, 17(1), 1-22. Article P01034. <https://doi.org/10.1088/1748-0221/17/01/P01034>

---

This material is protected by copyright and other intellectual property rights, and duplication or sale of all or part of any of the repository collections is not permitted, except that material may be duplicated by you for your research use or educational purposes in electronic or print form. You must obtain permission for any other use. Electronic or print copies may not be offered, whether for sale or otherwise to anyone who is not an authorised user.

PAPER • OPEN ACCESS

## Feasibility of neutral particle analysis for fast-ion measurements at W7-X

To cite this article: on behalf of the W7X-Team *et al* 2022 *JINST* 17 P01034

View the [article online](#) for updates and enhancements.

### You may also like

- [Measurement of the fast ion distribution using active NPA diagnostics at the Globus-M2 spherical tokamak](#)  
N N Bakharev, I M Balachenkov, F V Chernyshev et al.
- [Implementation of a 3D halo neutral model in the TRANSP code and application to projected NSTX-U plasmas](#)  
S S Medley, D Liu, M V Gorelenkova et al.
- [An improved strategy for transferring and adhering thin nanoporous alumina membranes onto conducting transparent electrodes for template assisted electrodeposition of high aspect ratio semiconductor nanowires with increased optical absorption](#)  
Harsimran S Bindra, A B V Kiran Kumar, Somnath C Roy et al.



The Electrochemical Society  
Advancing solid state & electrochemical science & technology

242nd ECS Meeting

Oct 9 – 13, 2022 • Atlanta, GA, US

Abstract submission deadline: **April 8, 2022**

Connect. Engage. Champion. Empower. Accelerate.

**MOVE SCIENCE FORWARD**



Submit your abstract



## Feasibility of neutral particle analysis for fast-ion measurements at W7-X

S. Bannmann,<sup>a,\*</sup> S. Bozhenkov,<sup>a</sup> S. Äkäslompolo,<sup>b</sup> P. Poloskei,<sup>a</sup> W. Schneider,<sup>a</sup> O. Ford<sup>a</sup> and R.C. Wolf<sup>a</sup> on behalf of the W7X-Team

<sup>a</sup>Max-Planck-Institut für Plasmaphysik,  
Wendelsteinstr. 1, 17491 Greifswald, Germany

<sup>b</sup>Department of Applied Physics, Aalto University,  
FI-00076, AALTO, Finland

E-mail: [sebastian.bannmann@ipp.mpg.de](mailto:sebastian.bannmann@ipp.mpg.de)

**ABSTRACT:** A preliminary study investigating capabilities of a planned but not yet installed neutral particle analyzer (NPA) [1, 2] system combined with a diagnostic neutral beam at Wendelstein 7-X (W7-X) [3] is presented. Additionally two NPAs viewing the neutral beam injection (NBI) [4] source 8 beam and using it as neutral source are studied. The main focus is laid on what information about NBI fast-ion slowing down distributions can be inferred from active NPA measurements when altering the magnetic configuration, plasma  $\beta$ , density, electron temperature or radial electric field. For an order of magnitude estimation of the passive signal a model for penetration of neutral hydrogen recycling from the first wall is implemented. For the active signal a diagnostic neutral beam injector was simulated using FIDASIM [5]. The fast-ion slowing down distributions were calculated with ASCOT [6].

The synthetic NPA signal is found in general to be sensitive to changes in the fast-ion distribution function. Distinct features can be seen in the high energy active signal in the high-mirror configuration when changing  $\beta$ , especially, when looking at deeply trapped fast particles. However, for the initially planned installation geometry of the NPA diagnostic most fast-ion distributions exhibit only small differences in the magnitude and especially shape. In a high density case in the standard magnetic configuration with a central  $\beta$  of 8%, the fast-ion density in the core region is too low to provide a measurable flux of charge exchanged neutrals. The passive signal from the inner plasma regions is found to be negligible compared to the active signal.

**KEYWORDS:** Simulation methods and programs; Nuclear instruments and methods for hot plasma diagnostics

\*Corresponding author.

---

## Contents

<b>1</b>	<b>Introduction</b>	<b>1</b>
<b>2</b>	<b>NPA modeling</b>	<b>3</b>
2.1	Neutral particle analysis	3
2.2	Fast-ion distribution functions	4
2.3	Model input	6
2.4	Model validation on Maxwellian plasma without fast-ions	9
<b>3</b>	<b>Results</b>	<b>10</b>
3.1	NPA signals with RuDiX as a neutral source	10
3.2	NPA signals with NBI Q8 as neutral source	14
<b>4</b>	<b>Conclusion</b>	<b>16</b>
<b>A</b>	<b>Neutral CX fluxes</b>	<b>18</b>

---

## 1 Introduction

When Deuterium (D) and Tritium (T) fuse in a thermonuclear fusion power plant  $\alpha$ -particles with kinetic energies much greater than the surrounding plasma are produced. They form a so called fast-ion population. Proper confinement of fast-ions is one of several necessities towards the success of a fusion power plant. The stellarator W7-X was optimized regarding fast-ion confinement and it is one of the major experimental goals to validate this feature [7]. Insufficient fast-ion confinement may lead to a damage of the first wall and deteriorates the power balance [8].

As no DT-operation is planned for W7-X and the device size and magnetic field are not suited for confining  $\alpha$ -particles, fast-ion studies will be performed primarily with fast-ions generated with auxiliary heating methods, such as neutral beam injection (NBI). At W7-X a NBI system of total 10 MW heating power is planned with an injection energy of 55 keV (60 keV) for H (D) beams [4]. In the last experimental campaign NBI sources 7 and 8 of a total of eight sources were active. In the next campaign sources 3 and 4 will be added. To study fast-ion confinement at W7-X and gain knowledge for future stellarator-type reactors the injection energy of 55 keV for hydrogen is chosen in such a way that the normalized Larmor-radius ( $\rho_L/a$ ) of injected fast-ions matches the one of  $\alpha$ -particles in a helical advanced stellarator (HELIAS) fusion reactor [9, 10].

One of the problems of the classical stellarator concept is that trapped particles are poorly confined as they drift radially outwards which is particularly deleterious for fast-ions because the magnetic drift scales with the energy [11]. A high collisionality helps to reduce fast particle losses in two ways: pitch-angle scattering can de-trap fast particles and a high collision frequency reduces the characteristic time scale on which fast-ions are slowed down to thermal speeds of the surrounding bulk plasma. From qualitative considerations it is clear that in a reactor fast-ions must be confined as

long as sufficient to thermalize them. Fast-ions with an energy of  $E \gtrsim 15T_e$  are dominantly slowed down by the plasma electrons through frictional drag and the following applies for the slowing down time:  $\tau_S \propto \frac{T_e^{3/2}}{n_e}$  [12]. The W7-X magnetic field was optimized for an improved collisionless fast-ion confinement and fast-ions in W7-X plasmas slow down to thermal speeds on a time scale of  $\tau_S \approx 0.1$  s (60 keV protons,  $n_e \approx 10^{20} \text{ m}^{-3}$ ,  $T_e \approx 4$  keV) [13]. Depending on the plasma parameters and magnetic configuration a fraction of them is lost before they can be thermalized. Due to the flexible coil current system W7-X has a freedom in magnetic configurations as described in [14]. The favorable configuration regarding the trapped fast-ion confinement is called the high-mirror configuration which has an increased magnetic mirror field ratio (maximum field strength divided by minimum field strength) compared to the so-called standard configuration and is achieved by adjusting the coil currents. In this configuration a factor of 2 reduction of collisionless losses is expected for a plasma  $\beta$  of 4% [13]. As confirming this expectation is one of the main experimental objectives this study investigates if the planned NPAs at W7-X are sensitive to that improvement. It is to be noted that the improved fast-ion confinement is very sensitive to the magnetic configuration and does not exist for other reference configurations, e.g. standard magnetic configuration. Additionally, an improved fast-ion confinement is expected in the presence of a negative radial electric field  $E_r$  as shown in [15].

Experimentally, there exist several diagnostic options for directly measuring fast-ion distribution functions [16], of which collective Thomson scattering (CTS) [17], fast-ion H/D- $\alpha$  (FIDA) spectroscopy [18, 19] and neutral particle analysis using a NPA are applicable to W7-X plasmas. A NPA measures neutral flux spectra of particles emerging from charge exchange (CX) reactions of fast-ions with neutral species. It can provide information about the fast-ion distribution function in a relatively small part of the fast-ion phase space but with a good energy resolution and good signal-to-noise ratio. For localized active NPA measurements an additional diagnostic neutral beam (RuDiX) is considered for installation at W7-X. The CX analysis and the simulation of passive (CX with recycling neutrals) and active (CX with beam neutrals) NPA signals at W7-X are studied in this paper for several synthetic fast-ion distributions computed with ASCOT [6, 20]. As there is currently no NPA installed at W7-X this study is a preliminary study, carried out to evaluate the planned NPA geometry regarding the assessment of fast-ion confinement in different magnetic configurations. Not only the configuration but also the electron density  $n_e$ , the electron temperature  $T_e$  and the radial electric field  $E_r$  are expected to influence the fast-ion confinement and thereby are also parameters which will be varied in this study to see the influence on the NPA signal. Finally, the aim of this study is to provide some reasoning if the planned NPA system including the diagnostic neutral beam injector is worth installing at W7-X for the named purpose.

To be able to do this a synthetic NPA model is implemented in Python. This choice has several advantages of which the most important are that Python is easy to learn and is extensively used throughout the scientific community. Especially for W7-X an easy access to existing webservices, e.g. for reading the wall geometry, is beneficial and made possible by easy to integrate Python libraries. To simulate the neutral beams and especially the halo a code called FIDASIM [5, 21] was used. This code was already successfully used at other experiments for synthetic NPA models, e.g. at AUG [22], DIII-D [23, 24] or LHD [25, 26]. At JET a NPA module implemented as part of the ASCOT suite of codes was used [27]. The main part of the model presented in the following section is similar to these studies. The main differences lie in the type of the installed or simulated detectors, the NBI systems of the different machines and the general plasma parameters.

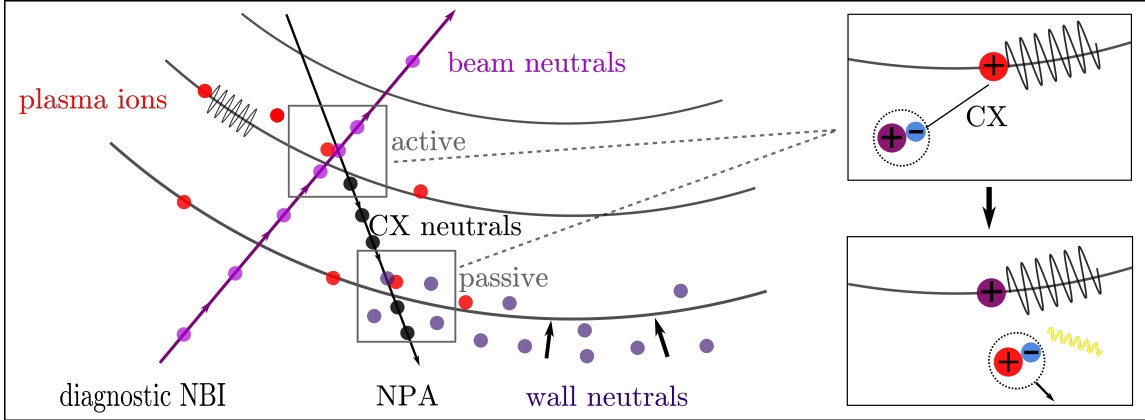


**Figure 1.** Charge exchange processes between diagnostic beam neutrals (RuDiX), recycled wall neutrals and plasma ions. The line of sight is marked with a black line going to the NPA.

This paper is structured in the following way: in [section 2](#) the implemented NPA model is explained including the underlying CX analysis and all essential input parameters. In [section 3](#) all obtained results are discussed.

## 2 NPA modeling

### 2.1 Neutral particle analysis

In a charge exchange (CX) process a bound electron is transferred from an atom to a bound state in another atom or ion [28]. In this study only hydrogen atoms and ions are considered so the CX reaction can be written as:  $\text{H} + \text{H}^+ \rightarrow \text{H}^+ + \text{H}^{(*)}$ . CX neutrals can leave the plasma and carry information about the velocity distribution function where they originate from. In the CX process the kinetic energies and momentum vectors of both ion cores are preserved. Measuring the flux of neutral particles produced by CX reactions of plasma bulk or fast ions with beam neutrals is called an active measurement, because the source of neutrals can be actively turned on and off. The flux originating from CX reactions with recycled neutrals coming from the first wall is called a passive measurement. The experimental situation is schematically drawn in figure 1.

The absolute CX neutral flux per second  $F$  arriving at the detector (NPA) in a velocity interval  $\Delta v_i$  is given by

$$F = \int dV P_{AB}(\vec{x}_{\text{Det}}, \vec{x}, v_i) \frac{dR(\vec{x}, v_i)}{dv_i} \Delta v_i. \quad (2.1)$$

In the volume integral all plasma volume visible to the detector must be included. The rate at which CX neutrals are generated at a point  $\vec{x}$  in the plasma is given by  $R$  and depends on the local ion and neutral densities and temperatures respectively. The probability of not being reionized on the way to the detector is given by  $P_{AB}$ . Detailed equations of these quantities are given in the appendix A. To compute the volume integrated CX fluxes coming from the visible part of the plasma to the detector as stated in eq. 2.1 a NPA forward model is implemented. The workflow of the simulation consists of several steps. First a cartesian grid is initialized containing the NPAs, RuDiX and the visible plasma. In the volume cells defined by the grid with a resolution of  $\approx 1$  cm

**Table 1.** Parameters for calculating fast-ion distributions. Density and temperature profiles are scaled by the given factor.  $E_r$  is the radial electric field. Configuration is referring to the magnetic configuration.

Case	Configuration	$n_e = n_i$	$T_e$	$T_i$	$E_r$	$\beta$ [%]	ID
1	standard					0.5	stdLow $\beta$
2	standard					4	stdHigh $\beta$
3	high-mirror					0.5	hmLow $\beta$
4	high-mirror					4	hmHigh $\beta$
5	standard	2×				0.5	2xNe
6	standard		2×			0.5	2xTe
7	standard				5×	0.5	5xEr
8	standard	2.5×	1.8×	1.8×		$\leq 8$	2.5ne1.8T

in each dimension all plasma parameters are taken to be constant. The chosen grid resolution is sufficient to capture the relevant plasma temperature and density profile information used for the calculation of the CX reaction rate. Using the full detector and vessel geometry all cells with a line of sight to the detector are found and the CX reaction rate is calculated in each one. CX reactions take place both with thermal plasma ions and fast-ions. The resulting rate is scaled with the solid angle of detector area visible from a volume cell. In the next step a line integral from each cell to the detector is computed to get the fraction of neutrals which are ionized on the way. The resulting neutral flux arriving at the detector is stored as the neutral flux spectrum.

## 2.2 Fast-ion distribution functions

To investigate the effect of varying fast-ion confinement properties on the NPA signal 8 fast-ion distributions are generated. They differ in magnetic configuration,  $\beta$ -value, radial electric field, electron temperature and electron density which are the parameters significantly influencing fast-ion confinement. The fast-ion distributions are provided by ASCOT as 5-dimensional distributions  $f(R, z, \varphi, \mu, E)$  for every single NBI source (the NBI system at W7-X consists of two boxes with four individual sources each, of which sources 3, 4, 7 and 8 will be operated in the next W7-X operation phase).

In table 1 an overview of the different cases is given. The location and magnitude of the beam ionization reactions, i.e. the birth of new fast-ions, depends on the local plasma density, beam density and the CX cross section. It can be described by a fast-ion birth profile which is the fast-ion generation rate (through beam ionizing reactions) over a radial coordinate. In spite of the dependence on plasma density the fast-ion birth profiles are kept constant in ASCOT except for the last case 8. This is done to isolate effects arising from the changes in parameters and not to be biased by changes in the birth profile (e.g. higher density increases fast-ion birth rate at the edge and decreases it in the core). In the last case 8 a consistent birth profile is used and the density and temperature scaling is self-consistent with the central  $\beta$ -value. Depending on the magnetic configuration different MHD-equilibria (calculated with VMEC [29]) are used.

In figure 2 all fast-ion distributions with parameters from table 1 are shown at a point close to the plasma center. Source 3 and 4 are summed for this plot. They inject at a pitch of  $\mu \approx -0.35 \pm 0.05$

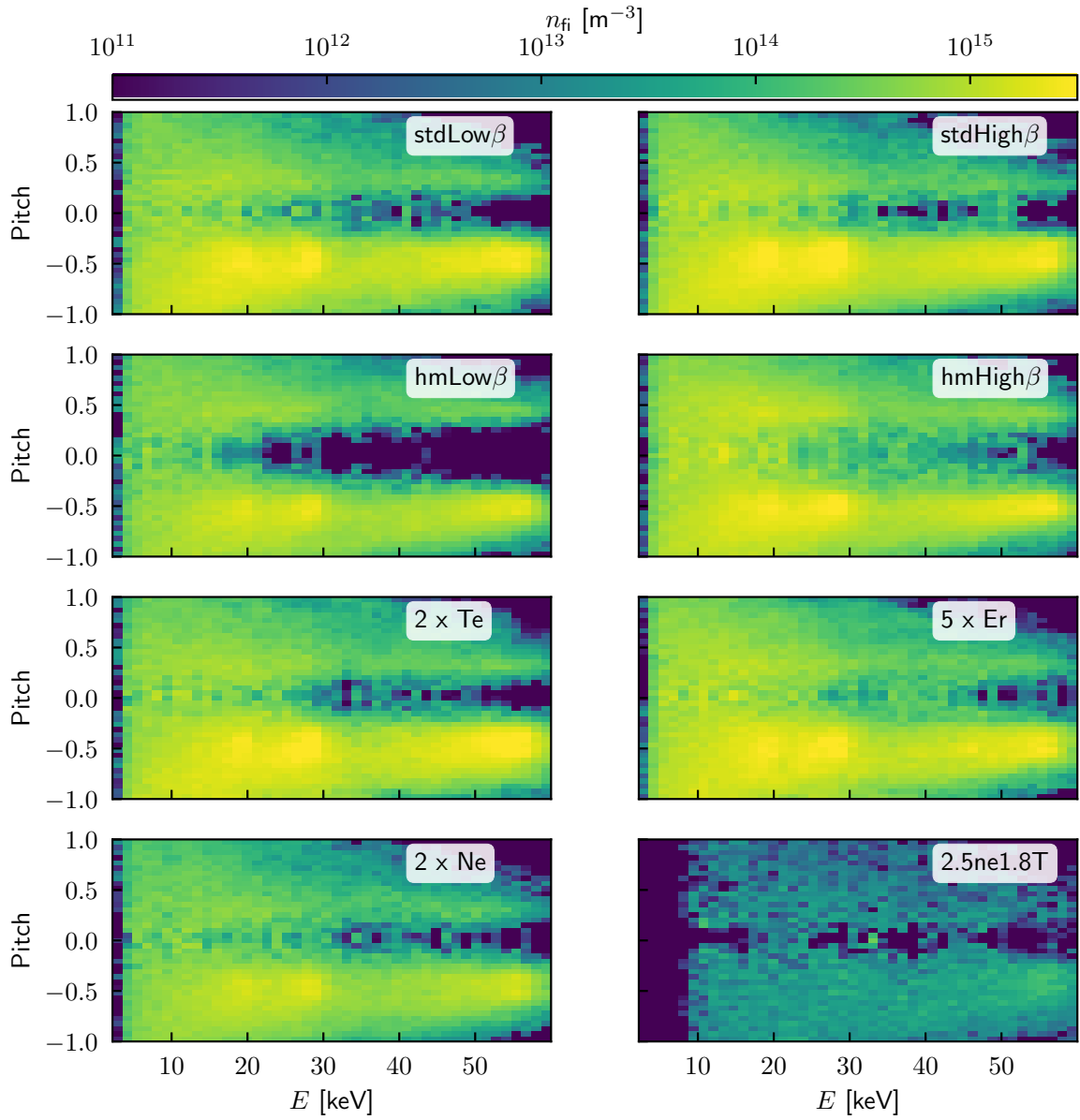


**Figure 2.** Fast-ion distributions at a point close to the plasma center for NBI sources 3 and 4 color plotted over energy and pitch. All plots have the same color axis limits.

( $-0.5 \pm 0.05$ ) which reflects the initial pitch angle of the born fast-ions. The injection energy of 55 keV is clearly visible except for the self consistent case with a central  $\beta$ -value of 8% (2.5ne1.8T). In this case the fast-ion birth profile was consistently computed and nearly no (at least compared to the other cases) fast-ions are born close to the core. Due to the high electron density a significant fraction of beam neutrals is ionized in a region closer to the edge. The NBI system not only accelerates single hydrogen but also hydrogen molecules ( $H_2$ ,  $H_3$ ) which after acceleration split up. As a consequence a fraction of the neutral hydrogen is injected with 55/2 keV and 55/3 keV respectively. This can also be seen in the distributions.

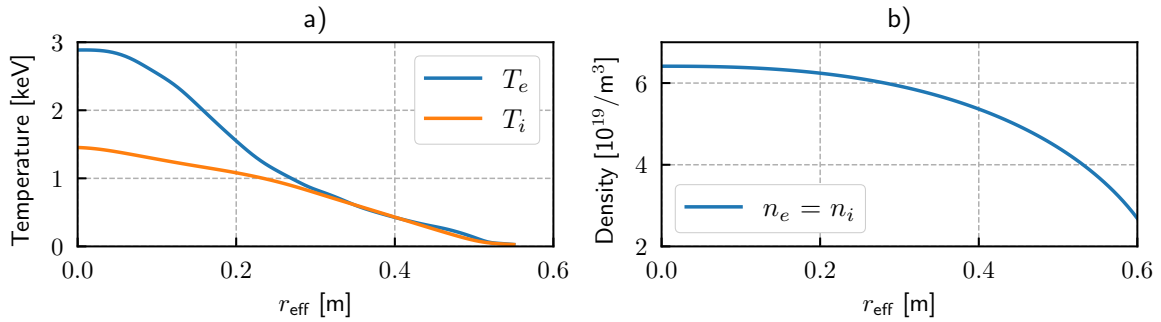


**Figure 3.** Typical temperature and density profiles as used for modeling. Electron and ion densities are assumed to be equal, i.e. no impurities are present.

### 2.3 Model input

The input essential for the calculation consists of the whole machine geometry, atomic collision rate coefficients and plasma parameter including equilibrium flux surfaces and profiles. To calculate CX reaction rates spatial distributions of injected beam neutrals and recycled neutrals from the first wall have to be provided.

**Atomic collisions.** The cross sections of CX reactions, ion impact ionization and electron impact ionization from the ground state for pure hydrogenic species are taken from [30]. They are used to compute the CX reaction rate and the reionizing probability in 2.1. Step wise excitation and ionization of CX neutrals is not taken into account but would, as estimated, decrease the total neutral flux arriving at the detector by about 15%, which is considered negligible for the purposes of this paper. The computed rate coefficients were also compared to effective data taken from the open ADAS website [31, 32]. Even though the ADAS coefficients account for stepwise ionization processes the differences to the ground state ionization rate coefficients were small enough to be ignored for this study. This is understood by realizing that the fraction of excited neutrals (beam and halo) is small at the investigated plasma parameters (< 1%).

**Magnetic field equilibrium and plasma profiles.** The needed 3D-MHD equilibria were computed with VMEC (Variational Moments Equilibrium Code) [29] and interfaced to the calculation via the W7-X VMEC webservice [33]. The used density and temperature profiles of electrons and ions are shown in figure 3. The plasma is assumed to be quasineutral and to be free of impurities (typical  $Z_{\text{eff}}$  values in the experiment are around 1.5), that is the ion and electron densities are equal.

**Detectors.** In total 4 detectors, i.e. 4 individual lines of sight, are investigated in this study. Two of them (NPA 1 and 2) with a viewing geometry on the RuDiX neutral beam and two (NPA 4 and 5) on the NBI source 8. The lines of sight of the NPAs and the neutral beam axis determine the localization of the active NPA signal and the visible pitch of the fast-ion distribution.

In figure 4b the planned geometry of NPA 1, 2 and RuDiX is shown. The neutral beam passes nearly radially through the plasma in a triangular section and intersects with the magnetic axis in the standard configuration. The beam injection and dump port are marked in the figure. The line of sight of NPA 1 intersects with the beam closer to the magnetic axis than NPA 2, meaning that the synthetic measurements of NPA 1 will be sensitive to the plasma core. The LOS of NPA 1 (2)

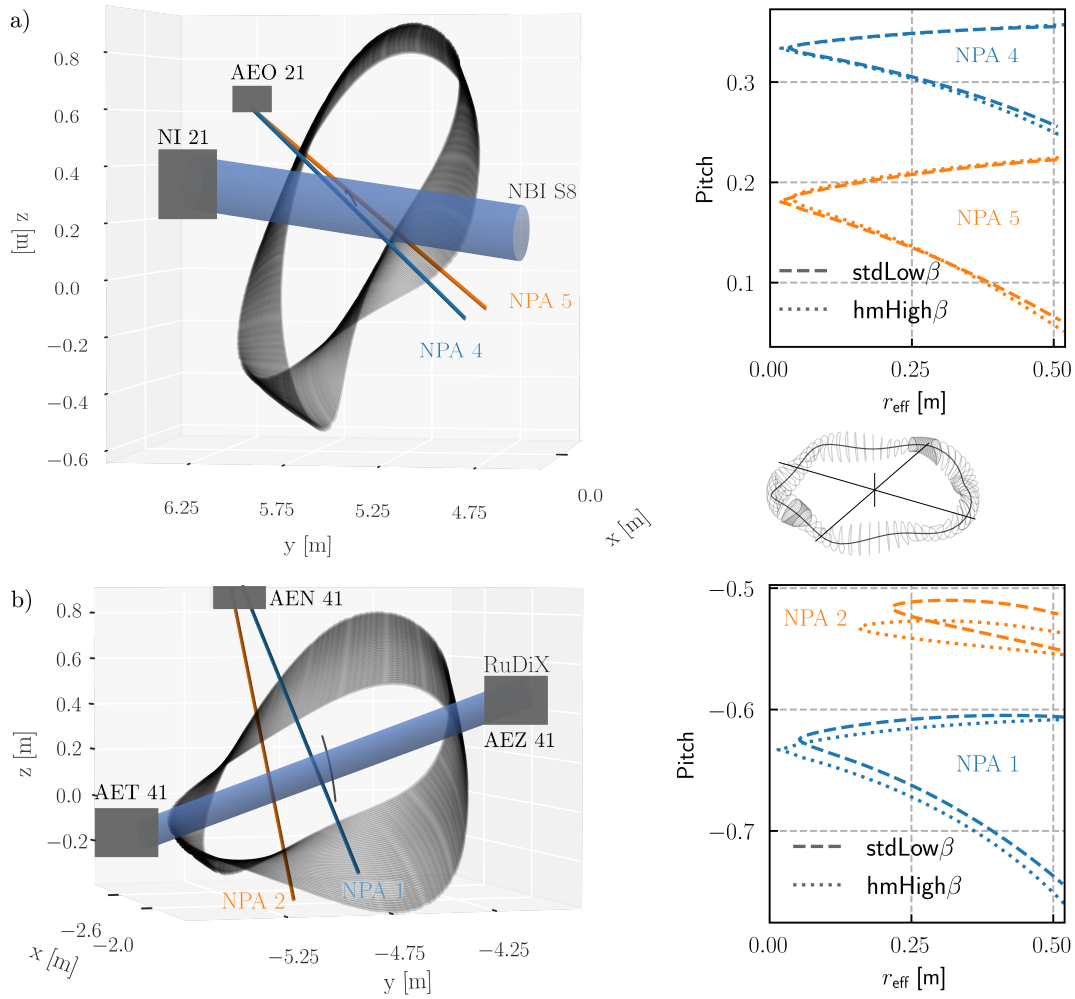


**Figure 4.** a: 3D geometry plot of NBI source 8 and the lines of sight of NPA 4 and 5. Right: for both NPAs the measured pitch when following its LOS through the plasma is plotted for two different magnetic configurations. Black contours show the last closed flux surfaces. b: 3D geometry plot of RuDiX and the lines of sight of NPA 1 and 2. Right: for both NPAs the measured pitch when following its LOS through the plasma is plotted for two different magnetic configurations. Black contours show the last closed flux surfaces.

intersects with the neutral beam at  $r_{\text{eff}} \approx 0.07$  m (0.20 m). These number vary slightly ( $\pm 10\%$ ) when changing the magnetic configuration or changing  $\beta$  as can be seen in the plot. NPA 1 measures at a more tangential pitch angle than NPA 2 when following its line of sight through the plasma. The range of measured pitch angles goes from  $\mu \approx -0.75$  to  $-0.6$  for NPA 1 and from  $\mu \approx -0.55$  to  $-0.52$  for NPA 2. Again this weakly varies with the configuration. Following the planned geometry of these devices the region of interest is the toroidal interval from  $\phi = 238^\circ$  to  $251^\circ$ . The foreseen NPAs for the just explained positions are ACORD-24 NPAs [2], for which, due to their size and weight, the viewing geometry can not be easily changed.

In figure 4a the investigated lines of sight of hypothetical NPA 4 and 5 in the NBI segment are shown. There were no preexisting plans for NPA measurements in the NBI segment and

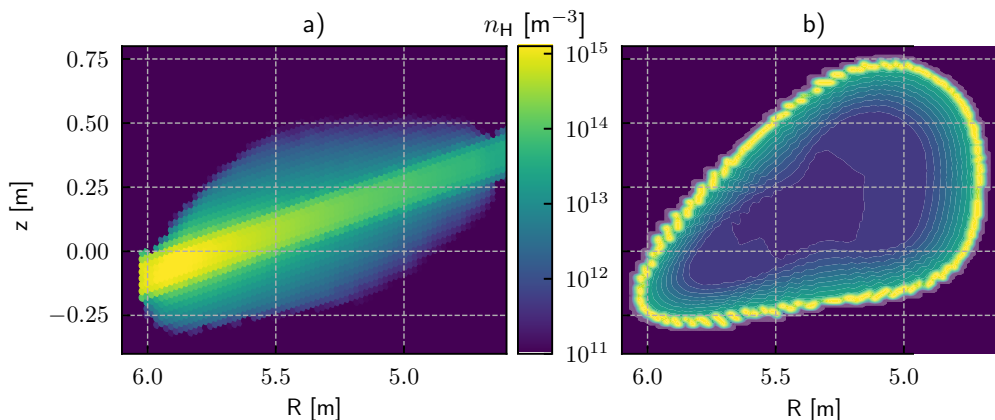


**Figure 5.** a: poloidal cut of neutral beam density for RuDiX along the beam axis. The beam enters the plasma at the bottom left corner. As a logarithmic color scale is used the halo is clearly visible around the beam. For this plot the 3 injection energy contributions of the beam are summed up. b: poloidal cut at a toroidal angle  $\varphi = 243^\circ$  of density of recycled neutral hydrogen diffusing from the first wall towards the magnetic axis.

the port chosen for this study provides a more perpendicular view on the neutral beam (source 7 and 8) than in the RuDiX case. Due to size restrictions only a compact NPA, e.g. the one tested at MAST [1], would be operable in this port. The LOS of NPA 4 (5) intersects with the neutral beam at  $r_{\text{eff}} \approx 0.14$  m ( $r_{\text{eff}} \approx 0.26$  m). The range of measured pitch angles goes from  $\mu \approx 0.05$  to 0.22 for NPA 5 and from  $\mu \approx 0.25$  to 0.33 for NPA 4. Both lines of sight intersect with the beam in the plasma core region.

The vessel geometry and wall intersection checks are provided by the W7-X webservice ComponentsDB and MeshSrv [33, 34].

**Diagnostic beam neutrals.** The diagnostic neutral beam injector has a power of 200 kW and the beam diameter is 13 cm. With these parameters initial neutral densities on the beam axis of up to  $10^{15} \text{ m}^{-3}$  are reached. The beam attenuation and the creation of a halo neutral distribution around the beam was calculated with FIDASIM [5, 21] and can be seen in figure 5a. This is primarily done to obtain sensible halo densities as the beam attenuation could be calculated with the implemented model as well (and agreed with the FIDASIM calculation). In the cases where the electron temperature or density is increased the neutral beam distribution was not consistently recalculated, thus the magnitude of the signal is overestimated in these cases. However, this does not alter the shape of the simulated NPA signals and is identical for every case.

**Recycling neutrals.** To get a rough estimate of the magnitude and even more importantly the localization of the passive signal a simple model of recycling neutrals is implemented. Assuming recycled hydrogen from the first wall to have room temperature the penetration length of these neutrals into a plasma with shown profiles (figure 3) would only be about 2 cm. However, one has to note that multiple CX processes can increase the penetration length substantially so that small fractions of neutrals can be found even in the core region [12]. In the implemented model

the assumption is made that the neutral influx is uniform on the whole LCFS and the total influx matches the outflux of particles (calculated from the average particle confinement time in a not actively fueled plasma). The flux of recycling neutral hydrogen per second per area is then

$$F_r = \frac{\int n_e dV_{\text{plasma}}}{S_{\text{plasma}} \tau_p} \quad (2.2)$$

where  $S$  is the plasma surface and  $\tau_p$  is the average particle confinement time. In figure 5b a poloidal cut of a recycled neutral distribution is shown. With the model assumptions significant neutral densities (of up to  $5 \times 10^{15} \text{ m}^{-3}$ ) are found only at the very plasma edge. Even when taking care of multiple CX processes the resulting neutral densities in the core region are by a factor of 10 to 100 smaller than the neutral densities created by the diagnostic neutral beam injector. The passive signal from the inner plasma region can therefore be neglected in active measurements. A recent study using the 3D-modeling tool EMC3-EIRENE combined with  $H\alpha$ -spectroscopy measurements agrees on the magnitude of the recycled neutral densities found with the presented simple model [35].

## 2.4 Model validation on Maxwellian plasma without fast-ions

In a plasma in thermal equilibrium and without any fast-ion species the maximum visible ion temperature can be deduced from a logarithmic fit of a passive CX flux spectrum [36]. This is possible due to the fact that most of the CX neutrals in the energy range from 5 to 12 keV originate from the plasma region with the highest ion temperature visible. The implemented NPA model is used to deduce the ion temperature in the described manner as a first test and sanity check. In figure 6 the calculated CX flux spectrum for the experimental temperature profile (as shown in figure 3) is plotted. As the ion temperature at the edge is quite low there is a high contribution to the CX flux at energies below 5 keV. The linear fit in the energy range from 7 to 12 keV yields a maximum ion temperature of 1.332 keV. With the simulated line of sight the maximum ion temperature visible is about 1.4 keV. The fitted temperature is a bit smaller due to attenuation effects in a dense plasma. This effect is to be expected and also described in [36]. It will also become clear after reading section 3.1 where the origin of the passive and active CX fluxes is studied. Overall, the resulting

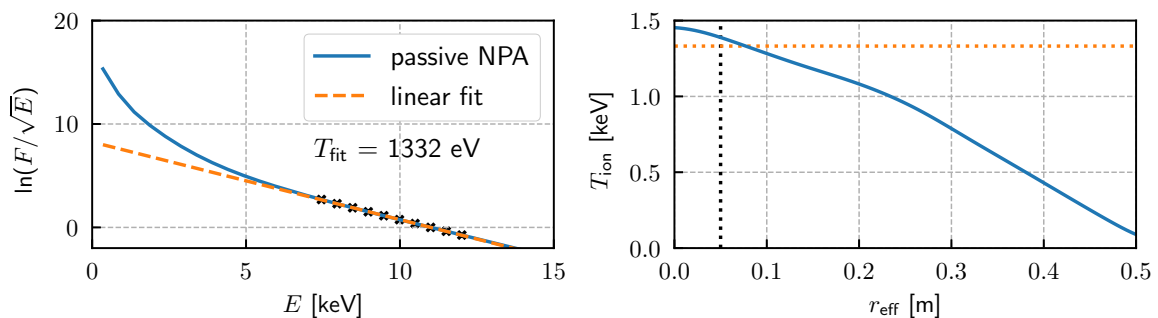


**Figure 6.** Passive CX flux spectrum without fast-ions for the experimental temperature profile. A linear fit of the logarithmic plot yields the maximum ion temperature of 1.332 keV. The difference to actual maximum ion temperature on the LOS is caused by attenuation effects in a dense plasma. The vertical line in the temperature profile marks the minimum effective radius  $r_{\text{eff}} \approx 0.05 \text{ m}$  visible to the NPA. The horizontal line marks the fitted ion temperature.

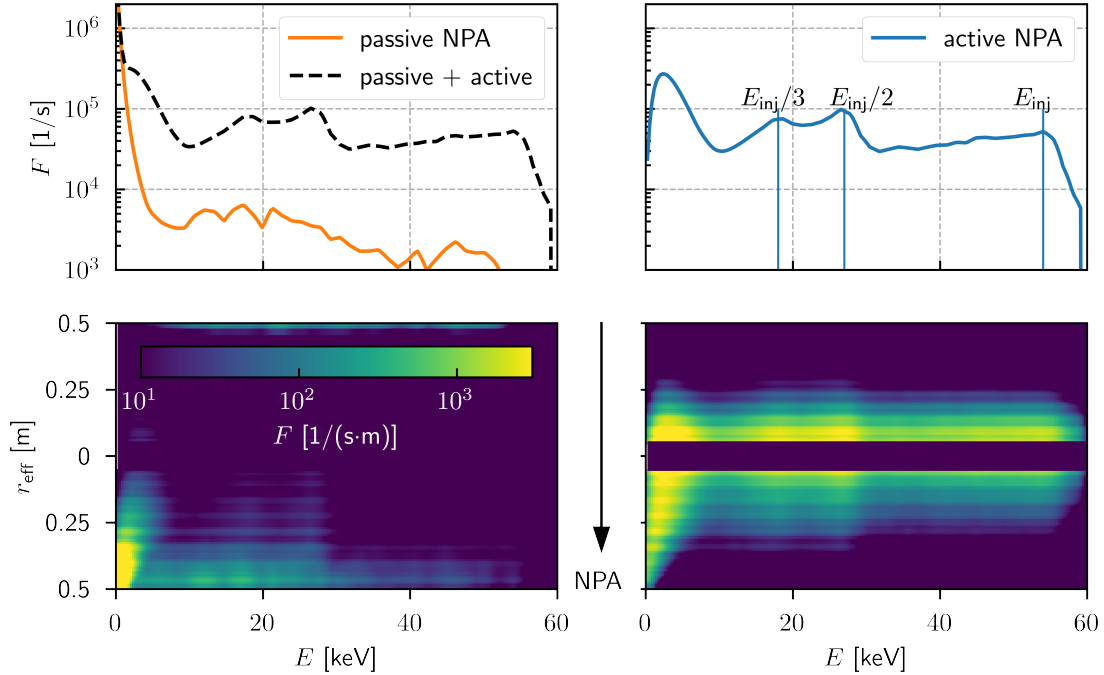


**Figure 7.** Top row: passive and active CX flux for NPA 1 and NBI sources 3, 4 for the standard magnetic configuration at  $\beta = 0.5\%$ . Bottom row: spatial origin of the corresponding neutral fluxes. The blue arrow indicates the direction the neutrals travel towards the NPA. Its LOS does not intersect with the magnetic axis.

CX flux spectra without fast-ions show exactly the expected features and the temperature fits are in perfect agreement with the theory.

### 3 Results

In this section the major results of the CX analysis with four different NPA geometries for varying fast-ion distribution functions are presented.

#### 3.1 NPA signals with RuDiX as a neutral source

The RuDiX diagnostic neutral beam injector is used as a neutral source for the active measurements. The volume integrated NPA signal is calculated in an energy range from 0 to 65 keV (as there are nearly no fast-ions found at higher energies) for all investigated fast-ion distribution functions described in table 1. Additionally, the fast-ion phase space is studied at selected points in the plasma to be able to evaluate the sensitivity of the planned NPA geometry.

In this section NBI sources 3 and 4 are used as fast-ion sources. As both NPAs (1 and 2) measure at negative pitch this leads to measuring trapped and passing fast-ions. Fast-ion diagnostics need to be sensitive to the plasma core region. Consequently, the first step is to validate that active measurements with the described NPA system have a reasonable spatial resolution and that the active signal is not exceeded by the passive signal from the edge.

In the top row of figure 7 the calculated passive and active CX flux spectrum for NPA 1 for the standard magnetic configuration and  $\beta = 0.5\%$  is plotted. At very low energies ( $E < 2$  keV) the passive

flux coming from reactions with recycled neutrals prevails. This is due to a high recycled neutral density close to the edge where the bulk plasma is cold (resulting in a high CX reactivity). Above 2 keV the CX flux from reactions with beam and halo neutrals strongly dominates the spectrum. All the flux in this energy range stems from CX fast-ions and the NBI injection energies are clearly visible at 54/27/18 keV. In contrast to the passive NPA the neutral flux from the active measurement decreases at very low energies. In the bottom row of figure 7 the spatial origin of the signal in terms of the effective radius  $r_{\text{eff}}$  is plotted. For the passive measurement in the left column one can see that nearly all the flux originates from a small plasma layer at the edge facing the detector ( $0.5 > r_{\text{eff}} > 0.35$  m). This helps to understand why one underestimates the maximum plasma temperature visible by fitting the low energy passive signal. The high energy tail of the signal comes from the plasma edge as well. There is no significant flux contribution from the opposite plasma edge, because nearly all CX neutrals generated there are reionized on the way through the plasma. Since substantial recycled neutral densities are only found close to the edge this localization of the CX flux is in accordance with the expectations. In the active case for energies above 10 keV all the flux comes from a plasma layer close to the core ( $r_{\text{eff}} < 0.07$  m), which is the effective radius where the NPA LOS and RuDiX beam intersect). As the NPA view cone does not cover the magnetic axis there is no flux coming from  $r_{\text{eff}} < 0.05$  m. At energies below 10 keV the flux origin for the active measurement smears out over a wider range of  $r_{\text{eff}}$ . This is possible only due to halo neutrals diffusing in the area around the beam. Still, one can see that a clearly pronounced peak at low energies comes from the inner plasma resulting in the opposing behaviour compared to the passive case. The low temperature edge of the plasma is not visible due to low halo neutral densities in this region. The peak at  $\approx 1.5$  keV comes from CX reactions with the inner high temperature bulk plasma.

Similarly for all other investigated configurations the relevant fast neutral signal comes from active measurements, thus originating from the intersection of the NPA line of sight with the diagnostic neutral beam. The spatial resolution is very good and not significantly influenced by the beam halo. It is ultimately limited by the beam diameter.

In the next step for both NPAs the simulated fast-ion distribution functions are compared at a point  $\vec{x}_m$  in the plasma where the maximum (peak) neutral flux contribution to the active signal comes from. The quantity used to compare the fast-ion distributions is

$$q_{c_1, c_2}(\vec{x}_m) = \frac{f_{\text{fi}}^{c_1}(\vec{x}_m)|_{\text{norm}}}{f_{\text{fi}}^{c_2}(\vec{x}_m)|_{\text{norm}}}, \quad (3.1)$$

where  $c_1$  and  $c_2$  are the different cases from table 1. The distributions are normalized to the peak at  $E_{\text{inj}}/2$ . Hence,  $q$  measures fractional differences in the shapes of the distributions.

In figure 8 the comparison of the fast-ion distribution functions in the high-mirror configuration for  $\beta = 0.5\%$  and  $\beta = 4\%$  is shown. At the investigated point in the plasma NPA 1 (2) measures a pitch of  $\mu \approx -0.62$  ( $-0.51$ ). It is clearly visible that in the high-mirror configuration at the measured pitch angle of both NPAs no distinct differences in the shape are apparent in the distribution functions. Significant fractional differences are found only at pitch values around zero. In this part of the fast-ion phase space trapped particles are located. When going to smaller pitch values the differences seem to increase but at the same time the noise increases as these are Monte-Carlo computed distributions.

Measuring improved fast-ion confinement when increasing  $\beta$  in the high-mirror configuration is one of the main aims. With the originally planned NPA geometries it seems challenging as the main

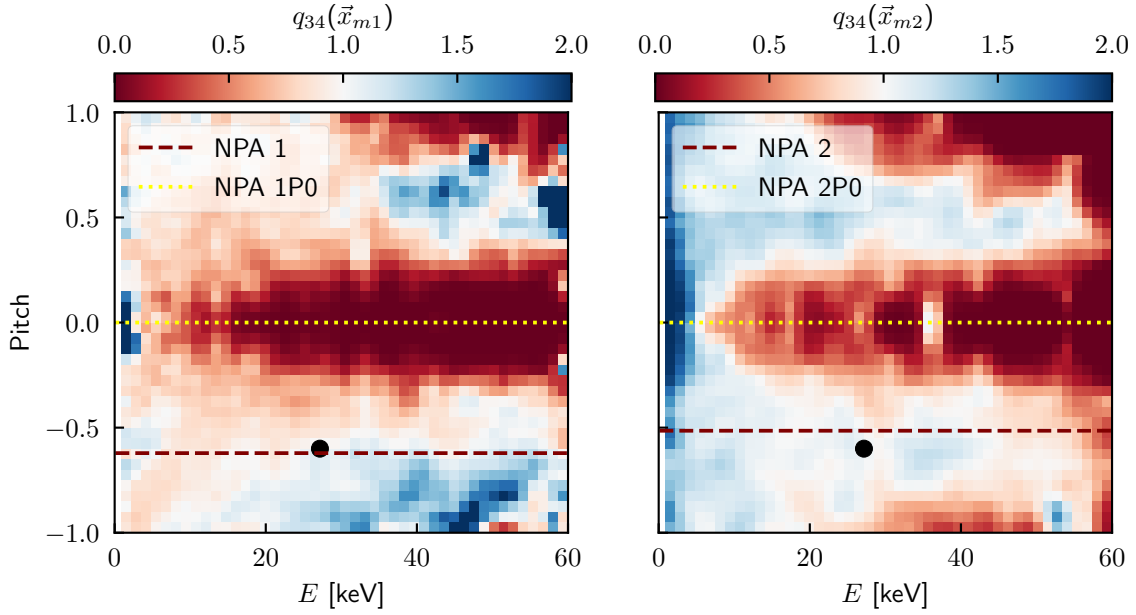


**Figure 8.** Color plot of ratio  $q$  of fast-ion distributions for  $\beta = 0.5\%$  and  $\beta = 4\%$  in the high mirror configuration. Both distributions are normalized to the peak at  $E_{\text{inj}}/2$  marked as black dot. Left: distributions evaluated at the point  $\vec{x}_{m1} = (-2.4, -4.8, 0.15)$  m,  $r_{\text{eff}} = 0.08$  m (point with the highest CX flux contribution to NPA 1). The dark red dashed line marks pitch visible to NPA 1 at this point and the yellow dotted line marks zero pitch chosen for NPA 1P0. Right: distributions evaluated at the point  $\vec{x}_{m2} = (-2.5, -5.0, 0.08)$  m,  $r_{\text{eff}} = 0.15$  m (point with the highest CX flux contribution to NPA 2). The dark red dashed line marks pitch visible to NPA 2 at this point and the yellow dotted line marks zero pitch chosen for NPA 2P0.

differences in the distributions become only visible at pitch values around 0 where deeply trapped particles are found. To assess how this difference may appear in the NPA signal two additional hypothetical detectors are set up: NPA 1P0 and NPA 2P0. For them the same position and alignment is used but during the CX calculation the fast-ion distribution is evaluated at  $\mu = 0$  at every point. Hence, this does not correspond to any planned or even possible (using the same port) NPA line of sight but is only done for analysing the sensitivity of the active CX signal to the fast-ion distribution functions.

The resulting, active neutral flux spectra for both NPAs and NBI sources 3 and 4 are shown in figure 9 (upper row: absolute flux, lower row: normalized flux). Except for the high density case  $2x\text{Ne}$  the absolute flux spectra measured by NPA 1 look very similar. No significant differences are visible in the signal when changing magnetic configuration,  $\beta$ , electron temperature or radial electric field while keeping the NBI birth profile constant. In the spectrum no major effects on the fast-ion confinement or slowing down behaviour are apparent at the measured pitch angle of NPA 1. Increasing only the plasma density ( $2x\text{Ne}$ ) the signal has a lower absolute flux, which is due to the higher reionization of CX neutrals leaving the plasma. The peak in the flux spectrum at  $E \approx 2$  keV is caused by CX reactions of beam neutrals with the bulk plasma. To compare the shapes of the measured spectra they are normalized to the Maxwellian bulk plasma peak. The relatively more pronounced peaks in the high density case are explained by the energy dependence of neutral ionization. Neutral fluxes below the beam energies are attenuated much faster. The absolute flux spectra measured by NPA 2 expose some differences in magnitude especially when changing the  $\beta$

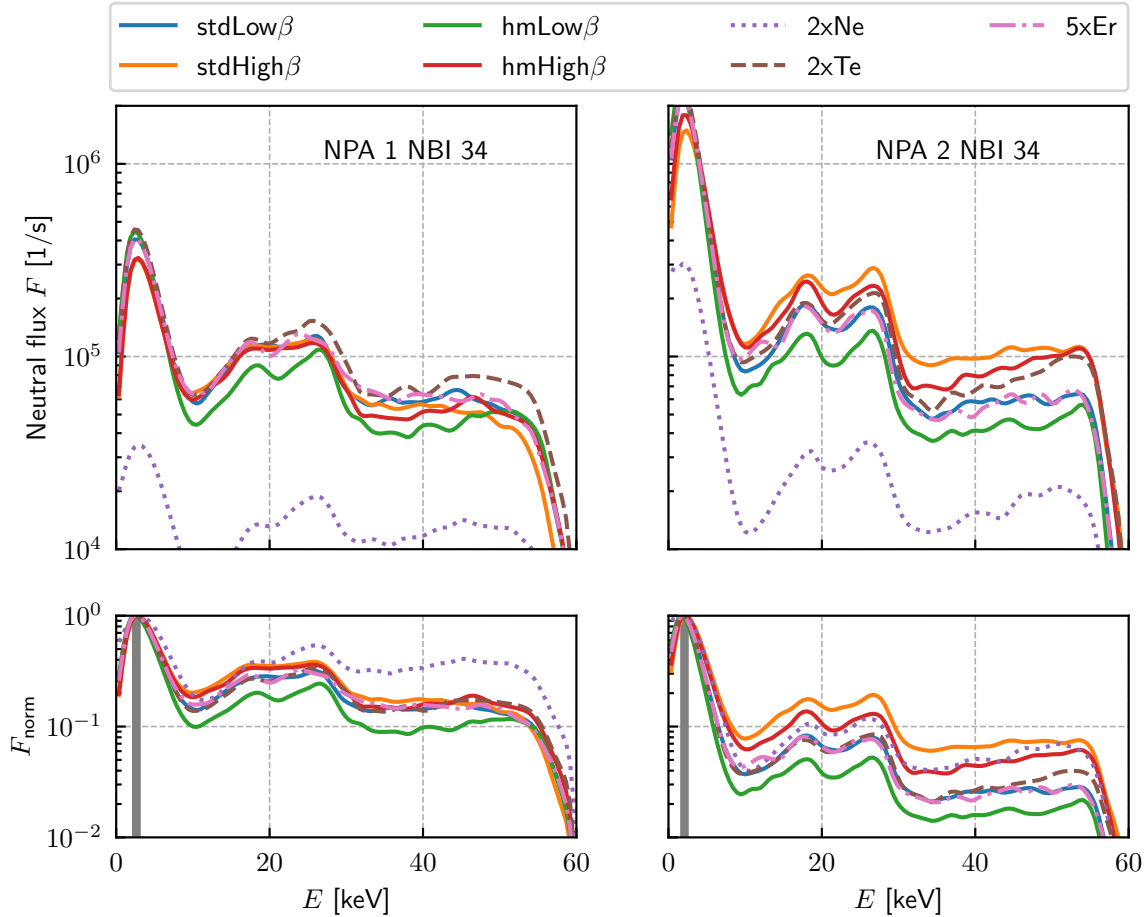


**Figure 9.** Synthetic CX spectra of active (with RuDiX diagnostic beam) NPA measurements using NBI sources 3 and 4 as fast-ion sources. In the upper row the absolute flux per second is plotted and in the lower row the flux normalized to the Maxwellian peak.

value. As NPA 2 measures closer to the edge the Maxwellian peak is sharper and higher compared to NPA 1. In the high-mirror configuration the fast-ion signal increases with  $\beta$  and also fractional differences in the shape are measurable. These results agree well with the expectations from the fast-ion phase space analysis and the sensitivity of NPA measurements to features of the fast-ion distribution functions. The distinction between the two high-mirror cases is expected to be best visible when going to smaller pitch values and measuring in the plasma center.

In figure 10 exactly these hypothetical 0 pitch measurements are shown. And indeed as expected from the fast-ion distribution function comparison there is a significant increase in the flux visible in the high-mirror configuration when increasing  $\beta$ . This change is not seen in the standard configuration. These results also support the assumption that NPA measurements are in general sensitive to features of the fast-ion distribution function.

The noise level is estimated from experimental NPA measurements at W7-AS with a similar detector type to be about  $2 \times 10^3$  1/s. The active signal of the studied cases is above this noise level over the whole energy range. The detector efficiency is not taken into account which would further decrease the measurable signal. For both NPAs the high temperature and high density case with

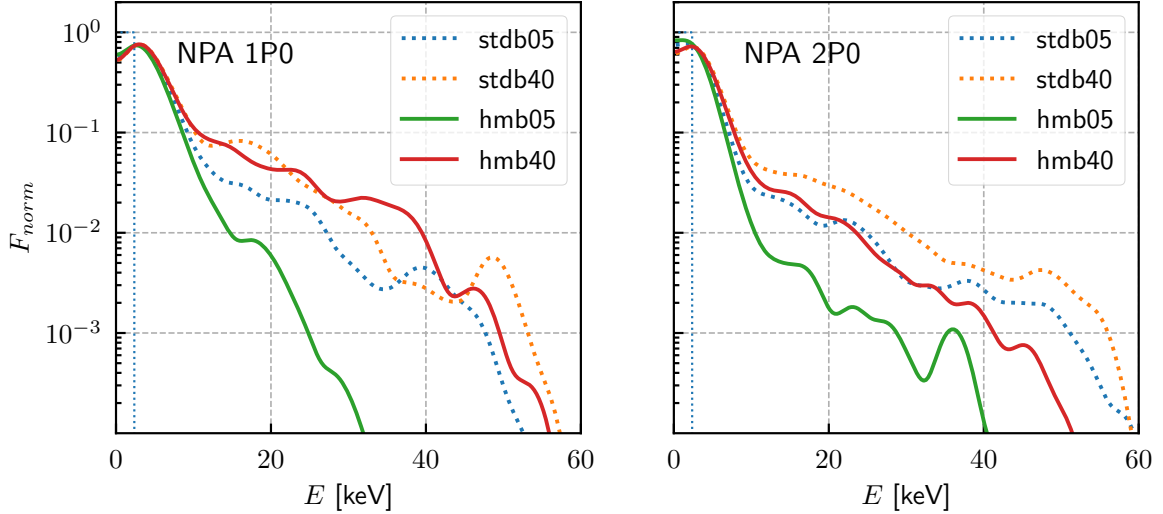


**Figure 10.** Synthetic CX spectra of active (with RuDiX diagnostic beam) NPA 1P0 and NPA 2P0 measurements using NBI sources 3 and 4 as fast-ion sources. In these calculations the fast-ion distribution functions were evaluated at  $\mu = 0$ .

a consistent fast-ion birth profile (2.5ne1.8T) do not lead to measurable (above estimated noise level) fast neutral fluxes. This is mainly due to very low fast-ion birth rates in the plasma core (see figure 2) in high density NBI operation and the high reionization of neutral fluxes leaving the plasma. Additionally the Maxwellian peak caused by CX reaction of beam neutrals with the bulk plasma ions becomes very broad and dominant. The noise can be reduced by higher integration times but, nevertheless, it may be a limitation for high density cases.

### 3.2 NPA signals with NBI Q8 as neutral source

Using the NBI itself as a neutral source is another option for active NPA measurements. The implemented model can easily be used to investigate this. Compared to the last section the viewing geometry and the neutral distribution has to be adapted. As already shown, the port AEO21 was identified to be physically available and suitable for an installation of a compact NPA and two lines of sight (called here NPA 4 and 5 respectively) are evaluated. In the light of the previous results lines of sight with small pitch angles were searched for. The LOS of NPA 4 (5) intersects exclusively with the NBI source 8 at an effective radius of  $r_{\text{eff}} \approx 0.14$  m (0.26 m). The beam attenuation and the halo formation were calculated the same way as for RuDiX with FIDASIM. Compared to RuDiX the NBI source 8 has a much higher power output. Combined with a bigger beam diameter this leads to a factor of 2 higher neutral densities on the beam axis throughout the whole plasma. The increased beam diameter also decreases the spatial resolution.

In figure 11 neutral flux spectra of NPA 4 and 5 are shown with NBI sources 7 and 8 being active. At the same time the NBI source 8 is used as the neutral source. For both LOS the neutral absolute flux over the whole energy range is significantly higher than in 9. This is explained mainly by the fact that the solid angle subtended by the CNPAs in the new investigated geometry is much larger than of the two previously studied NPAs (1 and 2). In addition to that the increased neutral densities especially on the beam axis further increase the signal. In both flux spectra no significant

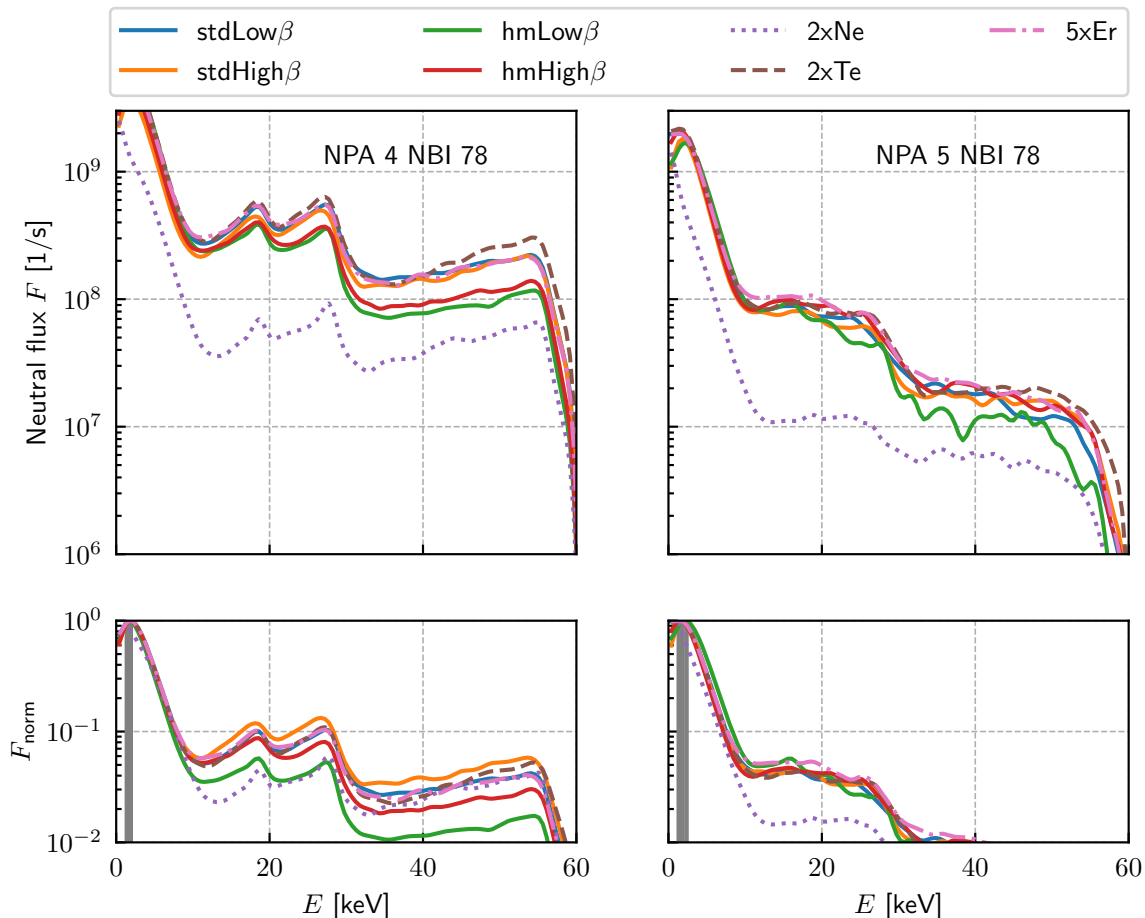


**Figure 11.** Synthetic CX spectra of active NPA measurements using NBI sources 7 and 8 as fast-ion sources and NBI source 8 as neutral source. In the upper row the absolute flux per second is plotted and in the lower row the flux normalized to the Maxwellian peak.

differences between the cases can be seen. Even though NPA 5 has a quite radial view ( $\mu \approx 0.1$ ) on the detected volume the differences in the high-mirror configurations are small. This result is puzzling when recalling that in the RuDiX segment there was a clear trend that a more perpendicular view on the magnetic surfaces improves the distinction between the high-mirror cases. To explain this behaviour one has to look again closely at the underlying fast-ion distribution functions.

In figure 12 the fast-ion distribution functions of the two high-mirror cases are compared at the points in the plasma where the maximum CX flux contribution to the NPAs comes from. As in the last section the distributions are normalized and compared regarding differences of the shape (see eq. 3.1). Most interestingly the results are quite different from the ones in the RuDiX segment. At both points the differences around 0 pitch are not as significant as in the other segment and also the behaviour at very tangential pitch angles is opposing the one obtained before. This leads to the conclusion that not only the measured pitch and the effective radius is important when choosing NPA lines of sight but also the magnetic cross section. The cause for that is likely the 3D structure of the magnetic field in a stellarator. At W7-X the magnetic field is stronger at the bean shaped cross section, that is close to the NBI plane, than at the triangular shaped cross section which leads to

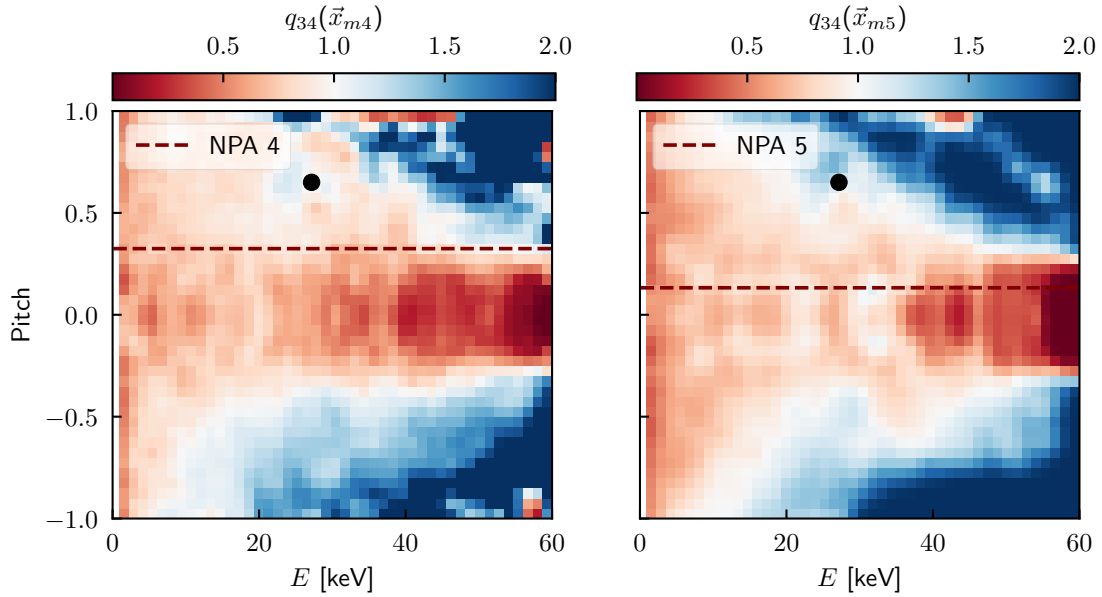


**Figure 12.** Color plot of ratio  $q$  of fast-ion distributions for  $\beta = 0.5\%$  and  $\beta = 4\%$  in the high mirror configuration. Both distributions are normalized to the peak at  $E_{\text{inj}}/2$  marked as black dot. Left: distributions evaluated at the point  $\vec{x}_{m4} = (0.035.520.24)$  m,  $r_{\text{eff}} = 0.14$  m (point with the highest CX flux contribution to NPA 4). The dark red dashed line marks pitch visible to NPA 4 at this point. Right: distributions evaluated at the point  $\vec{x}_{m2} = (-0.015.400.22)$  m,  $r_{\text{eff}} = 0.26$  m (point with the highest CX flux contribution to NPA 5). The dark red dashed line marks pitch visible to NPA 5 at this point.

the magnetic mirror effect. If there are no collisions the pitch angle of a particle decreases when going to weaker magnetic field periods as the particle gains in parallel velocity. Particles with small pitch values (thereby trapped particles) at the triangular cross section will not be apparent in the fast-ion distributions at the bean shaped cross section because their mirror field is much smaller and they are reflected before reaching it. Consequently, fast-ion distributions at different points in the plasma plotted over the pitch value are not directly comparable. These results not only confirm the sensitivity of NPA measurements again but also show the importance of carefully scanning the fast-ion phase space in the machine segment of interest before planning a NPA diagnostic at W7-X. The actual presented measuring geometries of NPA 4 and 5 do not seem to be suitable for assessing fast-ion confinement in the high-mirror or other configurations.

#### 4 Conclusion

In this paper the feasibility of fast-ion measurements with a NPA at W7-X was studied. For this, a forward model of the NPA diagnostic and of the neutral sources was developed and applied to compare synthetic signals for different magnetic configurations and plasma parameters. By interpreting CX neutral spectra, connections to the underlying fast-ion distribution can be drawn.

The developed model was used to calculate neutral fluxes originating from charge exchange processes between neutral populations (hydrogen) and bulk plasma ions and fast-ions in a pure hydrogen plasma. Two of the studied NPAs were originally planned at W7-X with a viewing geometry on the diagnostic neutral beam injector (RuDiX). Additionally, 2 not initially planned

NPA diagnostics with a viewing geometry on the NBI source 8 were investigated for a in theory feasible port. A simple model was implemented to estimate the recycling neutral influx from the first wall. The diagnostic neutral beams were modeled by a suite of codes called FIDASIM that correctly treats the halo neutrals [5]. Neutrals created by CX can be reionized on the way out of the plasma due to electron impact, ion impact and CX processes. The used plasma density and temperature profiles are typical for W7-X and are mapped to the effective radius using the VMEC magnetic equilibrium provided by a W7-X webservice. The subtended solid angle of the investigated detectors is Monte-Carlo computed in a far-field approximation. The investigated fast-ion distributions were calculated with the ASCOT code [6].

The synthetic NPA measurements are classified into two groups: passive and active measurements. In a passive measurement the neutral flux originating from CX processes between ions and recycled neutrals from the first wall is calculated. In an active measurement the same is calculated for ions and beam neutrals. Successful reconstruction of the maximum bulk plasma ion temperature from a passive NPA measurement by fitting of the logarithmic slope of the flux spectrum served as a simple model validation. It was found that significant recycled neutral densities are only present at the plasma edge. Consequently, most of the passive signal originates from there. An examination of the origin of the active signal confirmed that the registered CX reactions take place in the plasma core both for RuDiX and NBI Q8 as a neutral source.

Eight fast-ion distributions were generated for different magnetic configurations, density and temperature profiles, radial electric field and  $\beta$ . In seven cases the fast-ion birth profile was kept constant in the ASCOT code, to isolate effects on the fast-ion distributions to be measured with the NPAs. In one case with a high plasma density and temperature all plasma parameters were consistent and the birth profile was adapted as well.

The active charge exchange spectra showed that for the currently planned NBI sources 3 and 4, RuDiX and NPA 1 geometry no significant differences between the simulated fast-ion distributions can be measured. The active CX spectrum from NPA 2 which measures at a smaller pitch, however, showed an increase in magnitude of flux for the standard and high mirror magnetic configuration when going from  $\beta = 0.5\%$  to  $4\%$ . The shape of the signals did change slightly with  $\beta$ . For all seven cases with a fixed NBI birth profile the signals were above the detector noise level of 2 kHz. Only the case with the consistent NBI birth profile resulted in a very small signal below the noise level, due to the fact that in this case most of the NBI fast neutrals are ionized in the edge region so that in the core region, where the NPA 1 and 2 active CX flux originates from, nearly no fast-ions exist. Hence, high density plasmas ( $> 1e20 \text{ m}^{-3}$ ) pose a real problem to NPA measurements in the core as not only the fast-ion densities are low but also the signals are strongly attenuated. The reason that only small or no differences were apparent in the CX spectra was found to be that the underlying fast-ion distributions only had marginal differences at the measured pitch angles of  $\mu \approx [-0.65, -0.5]$ . At these pitch angles the investigated plasma parameter or magnetic configurations do not seem to strongly influence the fast-ion distribution function or the effects are not resolved by the ASCOT calculations. Since at these pitch angles only passing and shallowly trapped particles were measured, a hypothetical test case of two NPAs measuring at  $\mu = 0$ , thereby measuring deeply trapped particles, was set up. In this test case a strong difference in the magnitude and shape in the flux spectra in the high mirror configuration could be seen. When increasing  $\beta$  the flux of high energy neutrals significantly increased. An improved confinement of trapped fast-ions was expected for the high

mirror case, especially in the plasma core, and indeed could be seen with this hypothetical NPA setup. But it has to be emphasized that currently there is no such line of sight accessible with the NPA system.

Measuring in the NBI segment and using the NBI as fast-ion and neutral source even less differences between the cases were apparent. This came as a surprising result as the lines of sight in this segment were chosen to measure at small pitch values as supported by the results from the RuDiX segment. But it was found that in the NBI segment the differences between the fast-ion distribution functions at small pitch angles are less pronounced in the NBI segment which is likely due to the 3D structure of the magnetic field in W7-X.

Summarizing, NPA measurements at W7-X at the investigated plasma parameters are in general sensitive to features of fast-ion distributions and could be a valuable diagnostic option. At the proposed geometry of the NPAs viewing the diagnostic neutral beam changes in fast-ion slowing down behaviour and confinement caused by altering the radial electric field or electron temperature could not be measured. Some distinct features could be seen when changing plasma density, magnetic configuration and  $\beta$ . A more perpendicular NPA view line seems to be generally desirable. In the light of the obtained results it does not seem favorable to install RuDiX and the NPAs using the proposed geometry. Finding the optimal lines of sight by an extensive check of the fast-ion phase space in the plasma volume of interest and the use of a NPA which can cover more lines of sight could improve the situation. The investigated geometries of the NPAs viewing the NBI Q8 do not seem to be suited for assessing fast-ion confinement in any case. Before identifying new possible measuring geometries the fast-ion phase space should be scanned for optimal positioning of the detectors. Still this could prove an useful project as the NBI is already installed so the overall effort to get to NPA measurements is greatly minimized compared to using RuDiX.

## Acknowledgments

This work has been carried out within the framework of the EUROfusion Consortium and has received funding from the Euratom research and training programme 2014–2018 and 2019–2020 under grant agreement No. 633053. The views and opinions expressed herein do not necessarily reflect those of the European Commission.

## A Neutral CX fluxes

**CX reaction rate with bulk plasma.** For simplification the dependence of the reaction rates, densities and distribution functions on spatial coordinates  $\vec{x}$  is not written out in the following equations. The reaction rate  $R$  at which CX occurs between plasma ions and neutrals is:

$$R_{CX} = n_i \cdot n_n \int \int d\vec{v}_i d\vec{v}_n f_i(\vec{v}_i) \cdot f_n(\vec{v}_n) \cdot \sigma_{CX}(u) \cdot u \quad (\text{A.1})$$

$$u = |\vec{v}_i - \vec{v}_n|$$

This equation can be simplified by providing information about the velocity distribution function of neutrals for the passive and active measurement. The velocity distribution  $f_i$  of the bulk plasma is assumed to be Maxwellian as the plasma ions are in thermal equilibrium.

**Passive.** In the passive case we assume that the temperature of particles coming from the first wall is very small compared to the plasma temperature. Therefore, the neutral velocity distribution does not play an important role and can be approximated by a  $\delta$ -distribution. Assuming  $f_i(\vec{v}_i)$  to be constant on the solid angle  $\Omega_{\text{Det}}$  subtended by the NPA, one can easily transform into spherical coordinates.

$$R_{CX} = n_i n_n \Omega_{\text{Det}} \int_0^\infty dv_i f_i(v_i) \cdot v_i^3 \cdot \sigma_{CX}(v_i) \quad (\text{A.2})$$

**Active.** In the active case the neutrals consist of beam neutrals with 3 discrete energies  $E_b$  going in the direction of the beam axis  $\hat{e}_b$ . As the visible solid angle is small in the simulated NPA setup the relative velocity  $u$  can be assumed constant within this solid angle. Using this assumption one finds for the reaction rate with beam neutrals

$$R_{CX} = n_i n_n \Omega_{\text{Det}} \int_0^\infty dv_i f_i(v_i) \cdot v_i^2 \cdot \sigma_{CX}(u) \cdot u \quad (\text{A.3})$$

**CX reaction rate with fast-ions.** The fast-ion distribution function provided by ASCOT is given as a function of energy and pitch ( $\mu$ ). It is isotropic in the gyro-angle  $\varphi$  around magnetic field lines but is not isotropic in  $\mu$ . Generally, the reaction rate is written as

$$R_{CX} = n_n \int dE \int d\mu \int d\varphi \int d\vec{v}_n f_{fi}(E, \mu) \cdot f_n(\vec{v}_n) \cdot \sigma_{CX}(u) \cdot u \quad (\text{A.4})$$

Taking the definition of the solid angle one can establish a mapping between pitch and solid angle (dropping the minus sign).

$$d\Omega = \sin(\theta) d\theta d\varphi = d\mu d\varphi \quad (\text{A.5})$$

For the passive and the active cases  $f_n$  is the same as in A. The fast-ion distribution  $f_{fi}$  is assumed to be constant on the subtended solid angle  $\Omega_{\text{Det}}$ . The pitch angle  $\theta_0$  measured by the NPA is given by the angle between the line of sight vector and the magnetic field line. Explicitly, this gives for the passive reaction rate

$$R_{CX} = n_n \Omega_{\text{Det}} \int dE f_{fi}(E, \cos(\theta_0)) \cdot \sigma_{CX}(v_{fi}) \cdot v_{fi} \quad (\text{A.6})$$

and for the active one respectively

$$R_{CX} = n_n \Omega_{\text{Det}} \int dE f_{fi}(E, \cos(\theta_0)) \cdot \sigma_{CX}(u) \cdot u. \quad (\text{A.7})$$

**Attenuation of neutral fluxes.** The probability of a CX neutral to arrive at the plasma edge along a line parameterized by length  $l$  is given by [36]:

$$P_{AB} = \exp\left[-\int_A^B \alpha(l) dl\right] \quad (\text{A.8})$$

where  $\alpha$  is the full attenuation coefficient written as

$$\alpha = \frac{1}{v_n} [\langle \sigma_e v_e \rangle_{v_n} n_e + (\langle \sigma_p v_i \rangle_{v_n} + \langle \sigma_{cx} v_i \rangle_{v_n}) n_i]. \quad (\text{A.9})$$

### Cross sections of atomic collisions.

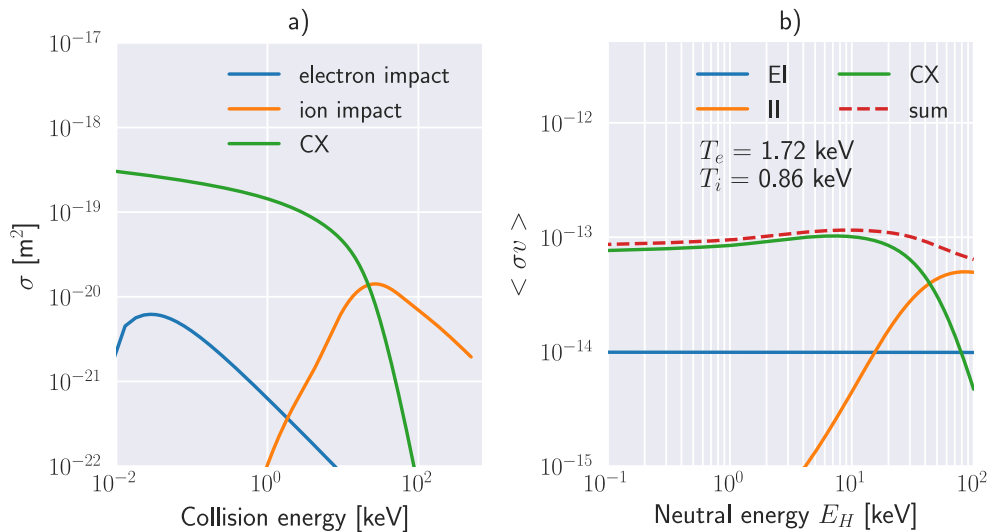


**Figure 13.** a: cross sections of ground state hydrogen ionizing reactions taken from [30]. b: Maxwell averaged rate coefficients.

### References

- [1] W. Schneider, M. Turnyanskiy, F. Chernyshev, V. Afanasyev, M. Kick and T. Richert, *Comparison of the IOFFE neutral particle analyser with the princeton analyser on the mega amp spherical tokamak*, *Vacuum* **83** (2008) 752 [Proceedings of the Symposium on Vacuum based Science and Technology, Greifswald, Germany, 5–7 September 2007].
- [2] F.V. Chernyshev, *Acord 24 ioffe website*, <http://www.ioffe.ru/ACPL/npd/npa01.htm>.
- [3] R.C. Wolf, C.D. Beidler, A. Dinklage, P. Helander, H.P. Laqua, F. Schauer et al., *Wendelstein 7-X program — demonstration of a stellarator option for fusion energy*, *IEEE Trans. Plasma Sci.* **44** (2016) 1466.
- [4] P. McNeely, M. Barlak, J. Baldzuhn, S. Bozhenkov, M. Drevlak, G. Gawlik et al., *Current status of the neutral beam heating system of W7-X*, *Fusion Eng. Des.* **88** (2013) 1034 [Proceedings of the 27th Symposium On Fusion Technology (SOFT-27), Liège, Belgium, 24–28 September 2012].
- [5] L. Stagner, B. Geiger and W.W. Heidbrink, *FIDASIM: A Neutral Beam and Fast-ion Diagnostic Modeling Suite*, <https://doi.org/10.5281/zenodo.1341369>.
- [6] E. Hirvijoki, O. Asunta, T. Koskela, T. Kurki-Suonio, J. Miettunen, S. Sipilä et al., *ASCOT: Solving the kinetic equation of minority particle species in tokamak plasmas*, *Comp. Phys. Commun.* **185** (2014) 1310.
- [7] T. Klinger, A. Alonso, S. Bozhenkov, R. Burhenn, A. Dinklage, G. Fuchert et al., *Performance and properties of the first plasmas of Wendelstein 7-X*, *Plasma Phys. Control. F.* **59** (2016) 014018.
- [8] S. Äkäslompolo, M. Drevlak, Y. Turkin, S. Bozhenkov, T. Jesche, J. Kontula et al., *Modelling of NBI ion wall loads in the W7-X stellarator*, *Nucl. Fusion* **58** (2018) 082010.

- [9] R.C. Wolf, A. Alonso, S. Äkäslompolo, J. Baldzuhn, M. Beurskens, C.D. Beidler et al., *Performance of Wendelstein 7-X stellarator plasmas during the first divertor operation phase*, *Phys. Plasmas* **26** (2019) 082504.
- [10] G. Grieger, W. Lotz, P. Merkel, J. Nührenberg, J. Sapper, E. Strumberger et al., *Physics optimization of stellarators*, *Phys. Fluids B* **4** (1992) 2081.
- [11] J. Faustin, W. Cooper, J. Graves, D. Pfefferlé and J. Geiger, *Fast particle loss channels in Wendelstein 7-X*, *Nucl. Fusion* **56** (2016) 092006.
- [12] R.J. Goldston and P.H. Rutherford, *Introduction to Plasma Physics*, Routledge (1995), ISBN 0-7503-0183-X.
- [13] M. Drevlak, J. Geiger, P. Helander and Y. Turkin, *Fast particle confinement with optimized coil currents in the W7-X stellarator*, *Nucl. Fusion* **54** (2014) 073002.
- [14] J. Geiger, C.D. Beidler, Y. Feng, H. Maaßberg, N.B. Marushchenko and Y. Turkin, *Physics in the magnetic configuration space of W7-X*, *Plasma Phys. Control. F.* **57** (2014) 014004.
- [15] Y.I. Kolesnichenko, V.V. Lutsenko, A.V. Tykhyy, A. Weller, A. Werner, H. Wobig et al., *Effects of the radial electric field on the confinement of trapped fast ions in the Wendelstein 7-X and Helias reactor*, *Phys. Plasmas* **13** (2006) 072504.
- [16] D. Moseev, M. Salewski, M. Garcia-Muñoz, B. Geiger and M. Nocente, *Recent progress in fast-ion diagnostics for magnetically confined plasmas*, *Rev. Mod. Plasma Phys.* **2** (2018) 7.
- [17] D. Moseev, M. Stejner, T. Stange, I. Abramovic, H.P. Laqua, S. Marsen et al., *Collective Thomson scattering diagnostic at Wendelstein 7-X*, *Rev. Sci. Instrum.* **90** (2019) 013503.
- [18] W.W. Heidbrink, K.H. Burrell, Y. Luo, N.A. Pablant and E. Ruskov, *Hydrogenic fast-ion diagnostic using Balmer-alpha light*, *Plasma Phys. Control. F.* **46** (2004) 1855.
- [19] B. Geiger, M. Garcia-Munoz, W.W. Heidbrink, R.M. McDermott, G. Tardini, R. Dux et al., *Fast-ion D-alpha measurements at ASDEX upgrade*, *Plasma Phys. Control. Fusion* **53** (2011) 065010.
- [20] S. Äkäslompolo, P. Drewelow, Y. Gao, A. Ali, C. Biedermann, S. Bozhenkov et al., *Validating the ASCOT modelling of NBI fast ions in Wendelstein 7-X stellarator*, *2019 JINST* **14** C10012.
- [21] B. Geiger, L. Stagner, W. Heidbrink, R. Dux, R. Fischer, Y. Fujiwara et al., *Progress in modelling fast-ion D-alpha spectra and neutral particle analyzer fluxes using FIDASIM*, *Plasma Phys. Control. F.* **62** (2020) 105008.
- [22] P.A. Schneider, H. Blank, B. Geiger, K. Mank, S. Martinov, F. Ryter et al., *A new compact solid-state neutral particle analyser at ASDEX upgrade: Setup and physics modeling*, *Rev. Sci. Instrum.* **86** (2015) 073508.
- [23] X. Du, M.V. Zeeland, W. Heidbrink and D. Su, *Development and verification of a novel scintillator-based, imaging neutral particle analyzer in DIII-d tokamak*, *Nucl. Fusion* **58** (2018) 082006.
- [24] X. Du, M.V. Zeeland, W. Heidbrink, L. Stagner, A. Wingen, D. Lin et al., *Resolving the fast ion distribution from imaging neutral particle analyzer measurements*, *Nucl. Fusion* **60** (2020) 112001.
- [25] M. Osakabe, M. Isobe, S. Murakami, S. Kobayashi, K. Saito, R. Kumazawa et al., *Fast-ion confinement studies on LHD*, *Fusion Sci. Technol.* **58** (2010) 131.
- [26] M. Isobe, M. Osakabe, T. Ozaki, M. Nishiura, P.V. Goncharov, E. Veshchev et al., *Fast-particle diagnostics on LHD*, *Fusion Sci. Technol.* **58** (2010) 426.
- [27] J. Varje, P. Sirén, H. Weisen, T. Kurki-Suonio, S. Äkäslompolo and J. contributors, *Synthetic NPA diagnostic for energetic particles in JET plasmas*, *2017 JINST* **12** C11025.

- [28] R.K. Janev, *Theory of Charge Exchange and Ionization in Ion-Atom (Ion) Collisions*, in *Atomic Processes in Electron-Ion and Ion-Ion Collisions*, F. Brouillard, ed., Springer US, Boston, MA (1986), ISBN 978-1-4684-5224-2, pp. 239–269.
- [29] S. Hirshman, W. van RIJ and P. Merkel, *Three-dimensional free boundary calculations using a spectral green's function method*, *Comp. Phys. Commun.* **43** (1986) 143.
- [30] R. K. Janev, D. Reiter, and U. Samm. *Collision processes in low-temperature hydrogen plasmas*, Tech. Rep., Berichte des Forschungszentrums Jülich 4105, Forschungszentrum Jülich (2003).
- [31] F. Guzmán, M. O'Mullane and H. Summers, *ADAS tools for collisional–radiative modelling of molecules*, *J. Nucl. Mater.* **438** (2013) S585 [Proceedings of the 20<sup>th</sup> International Conference on Plasma-Surface Interactions in Controlled Fusion Devices].
- [32] N. Badnell and M. O'Mullane, *OPEN-ADAS atomic data*, <https://open.adas.ac.uk/>.
- [33] M. Grahl, J. Svensson, A. Werner, T. Andreeva, S. Bozhnikov, M. Drevlak et al., *Web services for 3D MHD equilibrium data at Wendelstein 7-X*, *IEEE Trans. Plasma Sci.* **46** (2018) 1114.
- [34] S. Bozhnikov, J. Geiger, M. Grahl, J. Kießlinger, A. Werner and R. Wolf, *Service oriented architecture for scientific analysis at W7-X. an example of a field line tracer*, *Fusion Eng. Des.* **88** (2013) 2997.
- [35] V.R. Winters, F. Reimold, R. König, M. Krychowiak, T. Romba, C. Biedermann et al., *EMC3-EIRENE simulation of first wall recycling fluxes in W7-X with relation to H-alpha measurements*, *Plasma Phys. Control. F.* **63** (2021) 045016.
- [36] I.H. Hutchinson, *Principles of Plasma Diagnostics*, second edition, Cambridge University Press, Cambridge, U.K. (2009) [ISBN 0521803896].